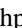






Self-induced inverse spin Hall effect in $\text{La}_{0.67}\text{Sr}_{0.33}\text{MnO}_3$ filmsPushpendra Gupta ¹, In Jun Park ², Anupama Swain ¹, Abhisek Mishra,¹ Vivek P. Amin,^{2,*} and Subhankar Bedanta ^{1,3,†}¹Laboratory for Nanomagnetism and Magnetic Materials, School of Physical Sciences, National Institute of Science Education and Research (NISER), An OCC of Homi Bhabha National Institute (HBNI), Jatni 752050, India²Department of Physics, Indiana University, Indianapolis 46202, USA³Center for Interdisciplinary Sciences (CIS), National Institute of Science Education and Research (NISER), An OCC of Homi Bhabha National Institute (HBNI), Jatni 752050, India (Received 14 October 2023; revised 10 January 2024; accepted 11 January 2024; published 29 January 2024)

The efficient generation of spin currents and spin torques via spin-orbit coupling is an important goal of spintronics research. One crucial metric for spin current generation is the spin Hall angle, which is the ratio of the spin Hall current to the transversely flowing charge current. A typical approach to measure the spin Hall angle in nonmagnetic materials is to generate spin currents via spin pumping in an adjacent ferromagnetic layer and measure the transverse voltage from the inverse spin Hall effect in the nonmagnetic layer. However, given that the spin Hall effect also occurs in ferromagnets, single ferromagnetic layers could generate a self-induced transverse voltage during spin pumping as well. Here we show that manganite-based $\text{La}_{0.67}\text{Sr}_{0.33}\text{MnO}_3$ (LSMO) films deposited by pulsed laser deposition exhibit a significant self-induced inverse spin Hall voltage while undergoing spin pumping. A spin pumping voltage of $1.86 \mu\text{V}$ is observed in the LSMO (12 nm) film. Using density functional theory and the Kubo formalism, we calculate the intrinsic spin current conductivities of these films and show that they are in reasonable agreement with the experimental measurements.

DOI: [10.1103/PhysRevB.109.014437](https://doi.org/10.1103/PhysRevB.109.014437)**I. INTRODUCTION**

Many spintronic applications depend on all-electrical control of magnetization dynamics. Such control can be achieved by electrically generating a spin current in a nonmagnetic layer that flows into a neighboring ferromagnetic layer and exerts a spin-orbit torque (SOT) [1–5]. The spin-transfer torque, or transfer of spin angular momentum to the ferromagnetic layer's magnetization, can result in magnetization switching in magnetic memories and self-sustained oscillations in spin torque oscillators. Thus an important step in achieving energy-efficient magnetization control is to optimize the efficiency of spin current generation.

It is well known that for nonmagnetic materials with appreciable spin-orbit coupling (for instance, heavy metals such as Pt or Ta), an applied electric field generates a spin current where the electric field, spin flow, and spin polarization are mutually orthogonal. This phenomenon, known as the spin Hall effect [6], is typically used as a spin current source in spintronic devices. Likewise, if a spin current with orthogonal spin flow and spin polarization flows into a heavy metal, a potential difference forms that is oriented perpendicularly to the spin flow and spin polarization. This process is known as the inverse spin Hall effect (ISHE). One prominent method to measure the strength of the inverse spin Hall effect in a nonmagnetic material is to generate a spin current via spin pumping [7–10] in a neighboring ferromagnetic material and measure the resulting inverse spin Hall voltage.

Both experimental [11–15] and theoretical [16–20] studies have shown strong evidence that single ferromagnetic layers also generate transversely flowing spin currents under an applied electric field. However, due to the lower symmetry of ferromagnets compared with nonmagnets, the electric field, spin flow, and spin polarization need not be mutually orthogonal. Spin current generation in single ferromagnet layers can be attributed to the spin Hall effect [15,21,22], the spin anomalous Hall effect [21,23,24], the spin planar Hall effect [16,23,25,26], and the magnetic spin Hall effect [18,20,27]. It is possible that some of the pumped spin current can flow into the ferromagnetic layer and be converted via the ISHE into a transverse voltage. To confirm this would require measuring an appreciable inverse spin Hall voltage while performing spin pumping in a single ferromagnet layer.

A recent report by Miao *et al.* shows that the injection of a pure spin current from yttrium iron garnet (YIG) to NiFe [permalloy (Py)] resulted in an ISHE in Py [11]. This report suggests the presence of appreciable spin-orbit coupling in the Py film, which is endorsed by the observation of an anisotropic magnetoresistance. Furthermore, Tsukahara *et al.* [12] have measured a self-induced ISHE in a single-layer Py film, i.e., without any adjacent high-spin-orbit-coupling material. These results indicate that the spin current generated within Py could be converted via the ISHE into a transversely oriented voltage. In addition, there are other studies of the intrinsic ISHE in Co and Fe films [14].

On a similar note, manganites such as $\text{La}_{0.67}\text{Sr}_{0.33}\text{MnO}_3$ (LSMO), which belongs to the family of complex oxides having ABO_3 structure, have attracted attention in recent years due to their multifunctionality and tunable properties [28]. The properties of complex oxides can be tuned by changing

*vpamin@iu.edu

†sbedanta@niser.ac.in

their compositions, thickness, strain, etc. [29,30]. Complex oxides can be grown epitaxially, which maximizes the electrical and structural performance. Recently, LSMO has gained much attention in spin-to-charge conversion studies due to its low damping, high Curie temperature ($T_C \sim 350$ K), and high spin polarization [31,32]. LSMO is an oxide-based ferromagnet that has been explored only as a spin current source in spin pumping studies [31,33–36]. In particular, in LSMO/Pt bilayers, antidamping-like spin torques have been observed [33], where the spin torques were primarily attributed to the spin Hall effect in Pt. However, to date, a self-induced inverse spin Hall effect has not been reported in manganites such as LSMO.

In this paper, we report a self-induced ISHE in epitaxial LSMO films under ferromagnetic resonance. Furthermore, we extract the intrinsic spin Hall conductivities of our LSMO films and compare them with first-principles calculations of the bulk spin Hall conductivity. The spin Hall conductivities extracted from both the experimental results and theoretical calculations are on the order of $10 \Omega^{-1} \text{cm}^{-1}$ and thus show reasonable agreement.

II. EXPERIMENTAL DETAILS

SrTiO_3 (100) [STO (100)]/LSMO (t nm) samples were deposited via the pulsed laser deposition technique using a laser of wavelength 248 nm and a vacuum chamber with base pressure 3×10^{-7} mbar. The samples are called samples SL1, SL2, and SL3 with thicknesses t of 12, 35, and 55 nm, respectively. For the growth of LSMO films, the substrate temperature was kept at 740°C during the deposition. Laser fluence and frequency were kept at 1.4 J/cm^2 and 2 Hz, respectively. The oxygen partial pressure during the growth was maintained at 0.47 mbar. Postdeposition annealing of the sample was performed at the same temperature (740°C) for 30 min at 250 mbar oxygen pressure. X-ray reflectivity (XRR) and x-ray diffraction (XRD) were performed with a diffractometer (Rigaku SmartLab) with wavelength $\lambda = 0.154$ nm. Cross-sectional high-resolution transmission electron microscopy (HR-TEM) was performed to check the epitaxy of deposited films by TEM (JEOL F-200). The dc magnetometry was performed using a magnetometer manufactured by Quantum Design (MPMS3) based on a superconducting quantum interference device (SQUID).

Coplanar-wave-guide-based (CPW-based) ferromagnetic resonance (FMR) spectroscopy (FMR spectrometer manufactured by NanOsc, Kista, Sweden) was carried out to study magnetization dynamics. The sample was kept on top of the CPW in a flip-chip manner [33,37]. To prevent shunting, a $25\text{-}\mu\text{m}$ polymer tape was placed between the sample and the CPW. A dc magnetic field H was applied perpendicular to the radio frequency field h_{rf} . ISHE measurement was performed at 7 GHz frequency and 25 mW microwave power. The voltage obtained due to ISHE was measured using a nanovoltmeter (Keithley 2182A).

III. RESULTS AND DISCUSSION

A schematic of the samples studied in this paper and the ISHE measurement are shown in Fig. 1(a). The XRD data

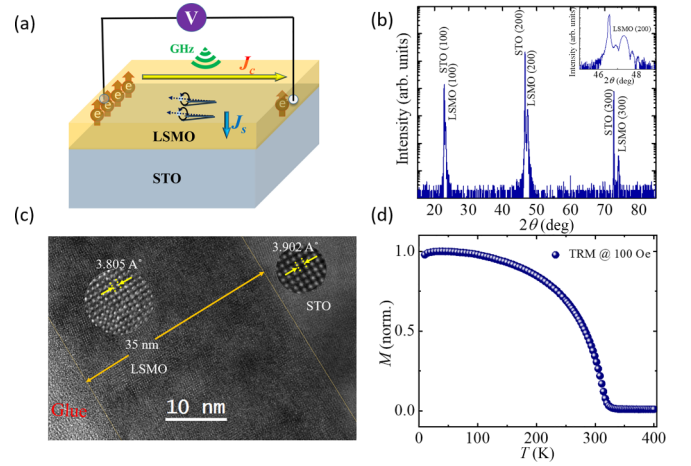


FIG. 1. (a) Schematic of sample geometry and ISHE measurement. (b) XRD pattern for sample SL2, in which LSMO film diffraction peaks are observed corresponding to STO (100) planes. A zoomed-in view of the (200) peak is shown in the inset. (c) HR-TEM image for sample SL2. The insets are the zoomed-in parts of LSMO films and STO substrate for measuring the lattice constants of LSMO and STO, respectively. (d) Thermoremanent magnetization (TRM) data in which the ferromagnetic-to-paramagnetic transition is observed at 320 K. Here, norm., normalized.

shown in Fig. 1(b) convey that the LSMO films were grown in (100) orientations, which is also the orientation of the STO substrate. This confirms that the LSMO films are highly epitaxial in nature. Film thickness was estimated using x-ray reflectivity (data not shown). Figure 1(c) depicts a cross-sectional HR-TEM image of sample SL2, which indicates the clear and sharp interfaces of STO/LSMO. The zoomed-in image confirms the epitaxial nature of LSMO.

Figure 1(d) shows the magnetization M vs temperature T plot for the LSMO (35 nm) sample. For this measurement, the sample was cooled from 400 to 5 K in the presence of a 100 Oe magnetic field. After cooling to 5 K, the magnetic field was switched off, and magnetization data were recorded with temperature. These protocols are called thermoremanent magnetization (TRM). From the figure, it can be clearly seen that the Curie temperature T_C of the deposited film is 320 K, which confirms the ferromagnetic phase of the sample at room temperature (300 K).

To study the magnetization dynamics, we have performed FMR spectroscopy from 3.5 to 10 GHz. The FMR spectra for all the samples are shown in Fig. 2. To calculate the Gilbert damping constant α , each FMR spectrum was fitted with the derivative of the standard Lorentzian equation. From the fitting of the FMR data, the resonance field H_{res} and linewidth ΔH have been extracted. The f vs H_{res} plots are shown in Fig. 3(a) for all the samples. The data are fitted using the Kittel equation

$$f = \frac{\gamma}{2\pi} \sqrt{(H_{\text{res}} + H_K)(H_{\text{res}} + 4\pi M_{\text{eff}} + H_K)}, \quad (1)$$

where γ ($= \frac{g\mu_B}{\hbar}$), g , μ_B , H_K , and M_{eff} are the gyromagnetic ratio, Landé g factor, Bohr magneton, in-plane anisotropic fields, and effective demagnetization, respectively.

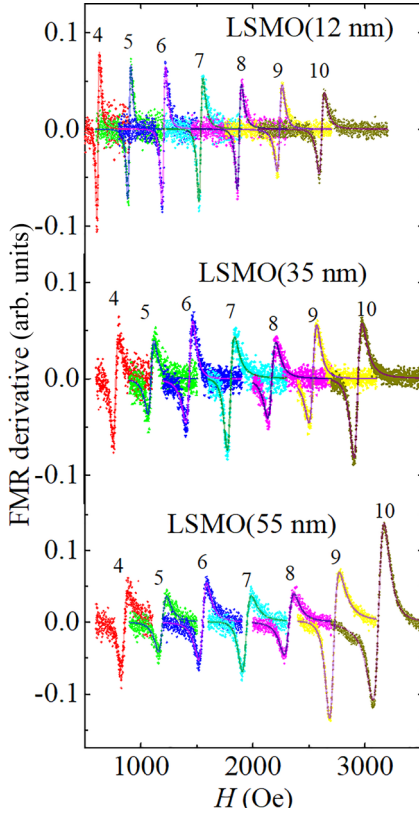


FIG. 2. FMR signal (solid circles) for different frequencies for samples SL1, SL2, and SL3. Solid curves are the fits using the Lorentzian equation.

Furthermore, the f vs ΔH data shown in Fig. 3(b) are fitted using the following linear equation:

$$\Delta H = \Delta H_0 + \frac{4\pi\alpha f}{\gamma}, \quad (2)$$

where ΔH_0 is the inhomogeneous linewidth. The values of the Gilbert damping constant α for samples SL1, SL2, and SL3 are evaluated to be 0.0086 ± 0.0002 , 0.0077 ± 0.0008 , and 0.0097 ± 0.0009 , respectively. The values of α match well with the previously reported values [38].

Furthermore, Gupta *et al.* have shown the presence of a significant anisotropic magnetoresistance in the LSMO/Pt system, which may arise due to the spin-orbit coupling of the LSMO film (though the adjacent Pt film could contribute via

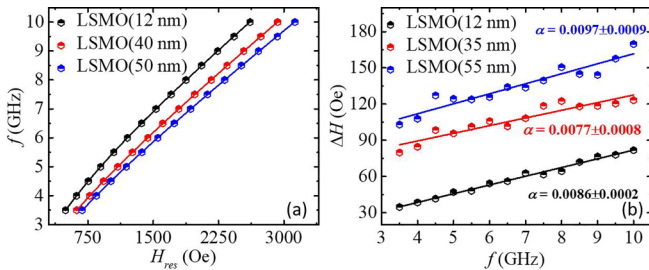


FIG. 3. Frequency f vs resonance field H_{res} plot and (b) linewidth ΔH vs f plot for STO/LSMO samples extracted from Fig. 2. Solid curves are the best fits for Eqs. (1) and (2).

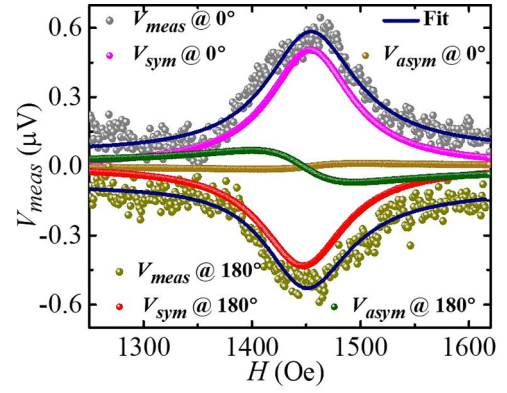


FIG. 4. Measured dc voltage V_{meas} vs field H measured at $f = 7$ GHz for sample SL1. The V_{sym} and V_{asym} components from V_{meas} have been separated using Eq. (4).

the proximity effect) [33]. The presence of spin-orbit coupling suggests there could be appreciable spin-to-charge conversion in the LSMO films. As LSMO shows metallic ferromagnetic behavior at room temperature, there is a possibility of an intrinsic ISHE in LSMO films similar to that found in the transition metal ferromagnets. The intrinsic ISHE causes a voltage across the sample transversely oriented to the spin flow, which is measured via making contacts with Cu wires from the sample to a nanovoltmeter. Figure 4 shows the measured voltage V_{meas} data at 0° and 180° . V_{meas} was fitted with Eq. (4) to separate out the symmetric (V_{sym}) and asymmetric (V_{asym}) contributions to the voltage [39]:

$$V_{\text{meas}} = V_{\text{sym}} \frac{(\Delta H)^2}{(H - H_{\text{res}})^2 + (\Delta H)^2} + V_{\text{asym}} \frac{(2\Delta H)(H - H_{\text{res}})}{(H - H_{\text{res}})^2 + (\Delta H)^2}. \quad (3)$$

From Fig. 4, it can be clearly seen that the V_{sym} component is more dominating than the V_{asym} component. Also, it can be noticed that V_{sym} changed its polarity when the sample was rotated 180° . This is a characteristic property that confirms the ISHE in LSMO films.

It is well known that V_{sym} mainly arises due to spin pumping, while the spin rectification effects integrated in anisotropic magnetoresistance (AMR), the anomalous Hall effect (AHE), etc., contribute to V_{asym} [39]. To calculate the spin pumping voltage from the measured voltage, a complete angle-dependent ISHE has been performed from 0° to 360° with a step of 5° . Each measured voltage data point is fitted to get V_{sym} and V_{asym} values using Eq. (4). Furthermore, V_{sym} and V_{asym} are plotted with their corresponding angles as shown in Figs. 5(a) and 5(b). The V_{sym} data are fitted using the equation [40]

$$V_{\text{sym}} = V_{\text{sp}} \cos^3(\phi + \phi_0) + V_{\text{AHE}} \cos(\phi + \phi_0) \cos \theta + V_{\text{sym}}^{\text{AMR}\perp} \cos(2(\phi + \phi_0)) \cos(\phi + \phi_0) + V_{\text{sym}}^{\text{AMR}\parallel} \sin(2(\phi + \phi_0)) \cos(\phi + \phi_0), \quad (4)$$

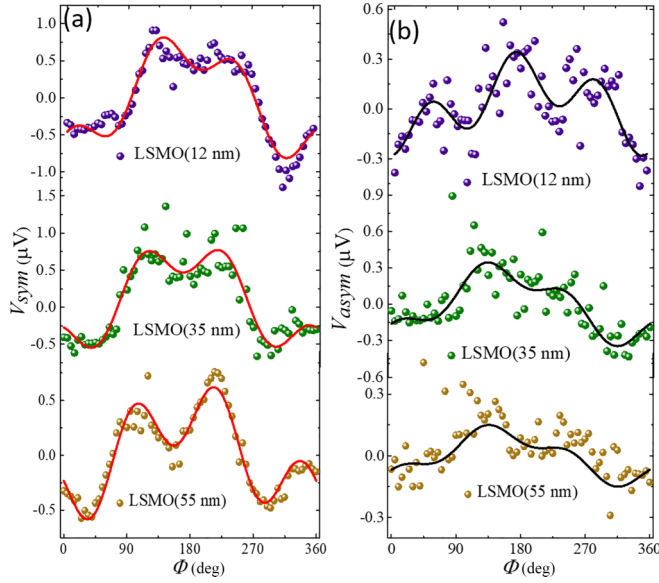


FIG. 5. (a) The ϕ -dependent V_{sym} and (b) V_{asym} for LSMO films. Red and black solid curves are the best fits for V_{sym} and V_{asym} , using Eqs. (4) and (5), respectively.

while the V_{asym} data are fitted using the equation [40]

$$\begin{aligned}
 V_{\text{asym}} = & V_{\text{AHE}} \cos(\phi + \phi_0) \sin \theta \\
 & + V_{\text{asym}}^{\text{AMR}\perp} \cos(2(\phi + \phi_0)) \cos(\phi + \phi_0) \\
 & + V_{\text{asym}}^{\text{AMR}\parallel} \sin(2(\phi + \phi_0)) \cos(\phi + \phi_0), \quad (5)
 \end{aligned}$$

where θ is the angle between the electric and magnetic fields of the applied microwave, which is 90° . The angle ϕ is defined as the angle between the voltage measurement direction and perpendicular to the magnetic field direction, while ϕ_0 is an extra factor to take care of the misalignment in the sample positioning. V_{AHE} is the anomalous Hall voltage, which arises due to the ferromagnetic (FM) nature of the sample. $V_{\text{asym}}^{\text{AMR}\perp,\parallel}$ and $V_{\text{asym}}^{\text{AMR}\parallel}$ are perpendicular (parallel) components of symmetric and asymmetric contributions to V_{AMR} and can be calculated using the following equation [40]:

$$V_{\text{AMR}}^{\perp,\parallel} = \sqrt{(V_{\text{asym}}^{\text{AMR}\perp,\parallel})^2 + (V_{\text{sym}}^{\text{AMR}\perp,\parallel})^2}. \quad (6)$$

From the fitting, significant spin pumping voltages have been obtained for the samples, which are listed in Table I. The value of V_{sp} dominates over any other spin rectification effects. As there is no high-spin-orbit-coupling (high-SOC) layer adjacent to the LSMO film, V_{sp} can be attributed to the intrinsic ISHE of LSMO films.

TABLE I. V_{sp} and V_{AHE} values (in microvolts) for all samples from the fitting of the data shown in Figs. 5(a) and 5(b) using Eqs. (4) and (5). V_{AMR} values were calculated using Eq. (6).

Sample	V_{sp}	V_{AHE}	V_{AMR}^{\perp}	$V_{\text{AMR}}^{\parallel}$
S1	1.86	0.12	1.43	0.39
S2	1.83	0.31	1.47	0.13
S3	1.39	0.12	1.31	0.15

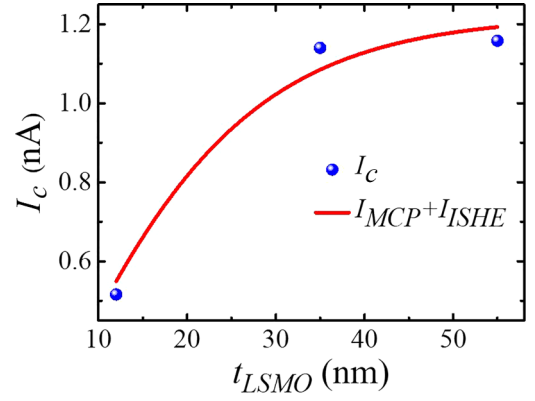


FIG. 6. Charge current I_c vs thickness (t_{LSMO}) of LSMO. The solid curve represents the fitting to $I_c = I_{\text{MCP}} + I_{\text{ISHE}}$, where I_{MCP} and I_{ISHE} are represented by Eqs. (7) and (8), respectively.

Furthermore, I_c vs t_{LSMO} data are plotted as shown in Fig. 6. As I_c has a contribution from magnonic charge pumping (I_{MCP}) and the inverse spin Hall effect (I_{ISHE}), the data have been fitted using the equation $I_c = I_{\text{MCP}} + I_{\text{ISHE}}$, where I_{MCP} and I_{ISHE} can be written in terms of the following expressions [41,42]:

$$\begin{aligned}
 I_{\text{MCP}} = & (\sigma_{\text{LSMO}} t_{\text{LSMO}} + \sigma_{\text{STO}} t_{\text{STO}}) w \\
 & \times \left(\frac{\Delta \rho}{2M_s^2} \right) \left(\frac{M_{\text{eff}} \gamma}{4\pi \alpha^2} \right) A^{(d)} h_{\text{rf}}^2, \quad (7)
 \end{aligned}$$

$$I_{\text{ISHE}} = \theta_{\text{SHA}} w \left(\frac{2e}{\hbar} \right) \lambda_{\text{LSMO}} \tanh \left(\frac{t_{\text{LSMO}}}{2\lambda_{\text{LSMO}}} \right) j_s^{\text{LSMO}}, \quad (8)$$

where θ_{SHA} , $\Delta \rho$, $A^{(d)}$, h_{rf} , and λ_{LSMO} are the spin Hall angle, anisotropic magnetoresistivity, spin-orbit coupling parameter, rf magnetic field of the microwave, and spin diffusion length, respectively. σ_{LSMO} , t_{LSMO} , σ_{STO} , and t_{STO} are the conductivity and thickness of the LSMO and STO layers, respectively. The spin current density at the LSMO/STO interface, j_s^{LSMO} , is given by [41,43]

$$j_s^{\text{LSMO}} = \frac{(g_r^{\uparrow\downarrow}) \gamma^2 h_{\text{rf}}^2 \hbar [4\pi M_s \gamma + \sqrt{(4\pi M_s \gamma)^2 + 4\omega^2}]}{8\pi \alpha^2 [(4\pi M_s \gamma)^2 + 4\omega^2]}. \quad (9)$$

From the above equation we have calculated the $g_r^{\uparrow\downarrow}$ value to be $1.2 \times 10^{16} \text{ m}^{-2}$, and j_s^{LSMO} has been considered as a fitting parameter. From the fitting of the I_c vs t_{LSMO} data shown in Fig. 6, the θ_{SHA} value is extracted as 0.33.

Finally, we have obtained the spin Hall conductivity using $\theta_{\text{SHA}} = \sigma_{\text{SH}}/\sigma_c$, where σ_{SH} and σ_c are the spin Hall conductivity and charge conductivity, respectively. The calculated values of σ_{SH} for samples SL1, SL2, and SL3 are 76.4, 58.9, and $50.0 \Omega^{-1} \text{ cm}^{-1}$, respectively.

In an earlier report, spin current has been generated in the Py layer itself via FMR due to the high resistivity of the adjacent SiO_2 layer, which prevents the spins from diffusing through it (the SiO_2 layer) [12]. A similar self-induced ISHE observation has also been made in Co and Fe films [14]. In our case, the resistivity of STO is comparatively less than that of SiO_2 [44]. When FMR occurs in the LSMO layer, the spin current is generated, which tends to move towards the LSMO/STO interface. At the interface, spins get scattered

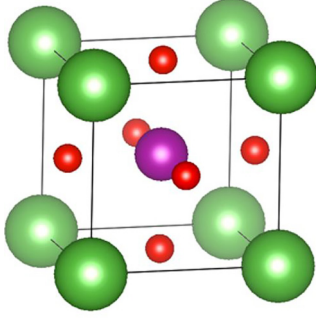


FIG. 7. Bulk crystal structure of perovskite LaMnO_3 or SrMnO_3 . The green, red, and purple spheres represent La (or Sr), O, and Mn atoms, respectively. A simpler model was chosen to reduce computational costs.

due to the charged impurities, which might be causing a spin gradient in the LSMO layer. This spin gradient creates spin current which gets converted into charge current via ISHE, which leads to the generation of potential difference.

It is noted that anisotropy may modify the spin pumping in FM/HS heterostructures, where HS refers to a material that exhibits high SOC. The anisotropy of the FM material can be modified due to strain which may arise due to lattice mismatch. In this context, from the HR-TEM image [Fig. 1(c)] a slight lattice mismatch between the STO substrate and the LSMO film is observed. Therefore one may expect a change in anisotropy due to strain. In this regard we have performed angle-dependent FMR measurements, which do not show any clear anisotropic behavior in the films (data not shown). Furthermore, the spin pumping voltages in the samples are comparable, which indicates that the impact of anisotropy is negligible for the studied LSMO films. Nevertheless, a detailed investigation is needed in future work to find the impact of anisotropy on self-induced spin pumping.

IV. COMPUTATION DETAILS

In order to evaluate the appreciable ISHE in LSMO from the experimental work, we performed density functional theory (DFT) calculations as implemented in the QUANTUM ESPRESSO package [45–47]. To reduce computational costs, we limited our theoretical calculation to LaMnO_3 (LMO) and SrMnO_3 (SMO), instead of LSMO, since LSMO requires a large unit cell in order to meet its chemical composition with symmetry and redundant calculations to average the disorder. The representative unit cell of LMO or SMO is shown in Fig. 7, where green, red, and purple spheres represent La (or Sr), O, and Mn atoms, respectively. Cutoff energies for the plane wave and charge density of 90 and 900 Ry and $9 \times 9 \times 9$ k -point grids were used to ensure that the total energy converged within 7×10^{-9} Ry. Once the ground states were obtained, we interpolated them into an orbital basis using the WANNIER90 package [48]. With the interpolated basis, the spin Hall conductivity tensor was calculated using Kubo's

TABLE II. Calculated nonzero spin Hall conductivity tensor elements of LMO and SMO, in $\Omega^{-1} \text{cm}^{-1}$.

Spin Hall conductivity	σ_{xyz}	σ_{yzx}	σ_{zxy}
LaMnO_3 ($M \parallel x$)	17.457	-18.671	14.547
LaMnO_3 ($M \parallel z$)	-18.677	14.558	14.471
SrMnO_3 ($M \parallel x$)	1.066	16.657	-3.595
SrMnO_3 ($M \parallel z$)	17.050	-3.638	-1.019

formula as implemented in [49,50]

$$\sigma_{\alpha\beta\gamma} = \frac{-e\hbar}{N_k V_c} \sum_k \sum_{n,m} (f_{nk} - f_{mk}) \times \frac{\text{Im}[\langle \psi_{nk} | \frac{1}{2} \{S^\gamma, v_\alpha\} | \psi_{mk} \rangle \langle \psi_{mk} | v_\beta | \psi_{nk} \rangle]}{(\epsilon_{nm} - \epsilon_{mk})^2 - (\hbar\omega + i\eta)^2}, \quad (10)$$

where α , β , and γ are the direction of the spin current, the electric field, and the spin polarization, respectively. We used $400 \times 400 \times 400$ k -point grids to calculate the spin Hall conductivity tensors of LMO and SMO.

For nonmagnetic materials, it is known that the nonzero elements of the spin Hall conductivity tensor can occur when the three components (i.e., α , β , and γ) are mutually orthogonal and they have the same magnitude. However, due to the lower symmetry from magnetization, ferromagnetic materials have different nonzero spin Hall conductivity components depending on the magnetization direction [27]. For instance, when the magnetization is parallel to the x direction, $\sigma_{xyz} = -\sigma_{xzy}$, $\sigma_{yzx} = -\sigma_{zyx}$, and $\sigma_{zxy} = -\sigma_{yxz}$, while when it is parallel to the z direction, $\sigma_{xyz} = -\sigma_{yxz}$, $\sigma_{yzx} = -\sigma_{xzy}$, and $\sigma_{zxy} = -\sigma_{zyx}$. Therefore we show our calculation results only for distinctive nonzero components (i.e., σ_{xyz} , σ_{yzx} , and σ_{zxy}), given in Table II. Clearly, there are nonzero values for the spin Hall conductivity tensor on the order of $10 \Omega^{-1} \text{cm}^{-1}$, which are of the same order as experimentally obtained values, although they are smaller than the ones from other perovskite structures ($\sim 100 \Omega^{-1} \text{cm}^{-1}$), such as SrIrO_3 [51], SrRuO_3 [52], BaOsO_3 , and SrOsO_3 [53], or Pt ($\sim 2000 \Omega^{-1} \text{cm}^{-1}$) [49]. We note that extrinsic mechanisms of the ISHE could also contribute to the experimental measurements but are not included in the theoretical calculations.

V. CONCLUSION

In summary, we measured a self-induced ISHE in highly epitaxial LSMO films and performed first-principles calculations of the spin Hall conductivities of bulk LSMO. The LSMO films were prepared using pulsed laser deposition and characterized by different techniques to confirm their epitaxial nature. The spin pumping voltage V_{sp} dominates over any other spin rectification effects in our samples, indicating the presence of appreciable spin-to-charge conversion in LSMO films. The spin Hall conductivity was calculated from first principles using density functional theory and the Kubo formalism, and the results qualitatively match our experimental findings. This study will help shed light on spin current generation in manganite-based films.

ACKNOWLEDGMENTS

S.B., P.G., A.M., and A.S. thank the Department of Atomic Energy (DAE) and the Science and Engineering Research Board (SERB), Government of India, for providing finan-

cial support. P.G. acknowledges UGC for support from an SRF fellowship. V.P.A. and I.J.P. acknowledge support from the National Science Foundation (NSF Grant No. DMR-2105219).

-
- [1] L. Liu, C.-F. Pai, Y. Li, H. W. Tseng, D. C. Ralph, and R. A. Buhrman, *Science* **336**, 555 (2012).
- [2] I. M. Miron, G. Gaudin, S. Auffret, B. Rodmacq, A. Schuhl, S. Pizzini, J. Vogel, and P. Gambardella, *Nat. Mater.* **9**, 230 (2010).
- [3] A. Manchon, J. Železný, I. M. Miron, T. Jungwirth, J. Sinova, A. Thiaville, K. Garello, and P. Gambardella, *Rev. Mod. Phys.* **91**, 035004 (2019).
- [4] V. P. Amin, P. M. Haney, and M. D. Stiles, *J. Appl. Phys.* **128**, 151101 (2020).
- [5] Q. Shao, P. Li, L. Liu, H. Yang, S. Fukami, A. Razavi, H. Wu, K. Wang, F. Freimuth, Y. Mokrousov, M. D. Stiles, S. Emori, A. Hoffmann, J. Åkerman, K. Roy, J.-P. Wang, S.-H. Yang, K. Garello, and W. Zhang, *IEEE Trans. Magn.* **57**, 1 (2021).
- [6] J. Sinova, S. O. Valenzuela, J. Wunderlich, C. H. Back, and T. Jungwirth, *Rev. Mod. Phys.* **87**, 1213 (2015).
- [7] O. Mosendz, J. E. Pearson, F. Y. Fradin, G. E. W. Bauer, S. D. Bader, and A. Hoffmann, *Phys. Rev. Lett.* **104**, 046601 (2010).
- [8] C. Hahn, G. de Loubens, M. Viret, O. Klein, V. V. Naletov, and J. Ben Youssef, *Phys. Rev. Lett.* **111**, 217204 (2013).
- [9] F. D. Czeschka, L. Dreher, M. S. Brandt, M. Weiler, M. Althammer, I.-M. Imort, G. Reiss, A. Thomas, W. Schoch, W. Limmer, H. Huebl, R. Gross, and S. T. B. Goennenwein, *Phys. Rev. Lett.* **107**, 046601 (2011).
- [10] J.-E. Wegrowe and H.-J. Drouhin, *Entropy* **13**, 316 (2011).
- [11] B. F. Miao, S. Y. Huang, D. Qu, and C. L. Chien, *Phys. Rev. Lett.* **111**, 066602 (2013).
- [12] A. Tsukahara, Y. Ando, Y. Kitamura, H. Emoto, E. Shikoh, M. P. Delmo, T. Shinjo, and M. Shiraishi, *Phys. Rev. B* **89**, 235317 (2014).
- [13] A. M. Humphries, T. Wang, E. R. J. Edwards, S. R. Allen, J. M. Shaw, H. T. Nembach, J. Q. Xiao, T. J. Silva, and X. Fan, *Nat. Commun.* **8**, 911 (2017).
- [14] K. Kanagawa, Y. Teki, and E. Shikoh, *AIP Adv.* **8**, 055910 (2018).
- [15] W. Wang, T. Wang, V. P. Amin, Y. Wang, A. Radhakrishnan, A. Davidson, S. R. Allen, T. J. Silva, H. Ohldag, D. Balzar, B. L. Zink, P. M. Haney, J. Q. Xiao, D. G. Cahill, V. O. Lorenz, and X. Fan, *Nat. Nanotechnol.* **14**, 819 (2019).
- [16] V. P. Amin, J. Zemen, and M. D. Stiles, *Phys. Rev. Lett.* **121**, 136805 (2018).
- [17] D. Go, F. Freimuth, J.-P. Hanke, F. Xue, O. Gomonay, K.-J. Lee, S. Blügel, P. M. Haney, H.-W. Lee, and Y. Mokrousov, *Phys. Rev. Res.* **2**, 033401 (2020).
- [18] A. Mook, R. R. Neumann, A. Johansson, J. Henk, and I. Mertig, *Phys. Rev. Res.* **2**, 023065 (2020).
- [19] Y. Yahagi, D. Miura, A. Sakuma, and J. Železný, *Phys. Rev. B* **104**, 094417 (2021).
- [20] L. Salemi and P. M. Oppeneer, *Phys. Rev. B* **106**, 024410 (2022).
- [21] V. P. Amin, J. Li, M. D. Stiles, and P. M. Haney, *Phys. Rev. B* **99**, 220405(R) (2019).
- [22] Y. Omori, E. Sagasta, Y. Niimi, M. Gradhand, L. E. Hueso, F. Casanova, and Y. C. Otani, *Phys. Rev. B* **99**, 014403 (2019).
- [23] T. Taniguchi, J. Grollier, and M. D. Stiles, *Phys. Rev. Appl.* **3**, 044001 (2015).
- [24] K. S. Das, W. Y. Schoemaker, B. J. Van Wees, and I. J. Vera-Marun, *Phys. Rev. B* **96**, 220408(R) (2017).
- [25] C. Safranski, E. A. Montoya, and I. N. Krivorotov, *Nat. Nanotechnol.* **14**, 27 (2019).
- [26] C. Safranski, J. Z. Sun, J.-W. Xu, and A. D. Kent, *Phys. Rev. Lett.* **124**, 197204 (2020).
- [27] A. Davidson, V. P. Amin, W. S. Aljuaid, P. M. Haney, and X. Fan, *Phys. Lett. A* **384**, 126228 (2020).
- [28] H.-U. Habermeier, *Mater. Today* **10**(10), 34 (2007).
- [29] H. Lu, T. A. George, Y. Wang, I. Ketsman, J. D. Burton, C.-W. Bark, S. Ryu, D. Kim, J. Wang, C. Binck, P. A. Dowben, A. Sokolov, C.-B. Eom, E. Y. Tsymlal, and A. Gruverman, *Appl. Phys. Lett.* **100**, 232904 (2012).
- [30] C. Kwon, M. Robson, K.-C. Kim, J. Gu, S. Lofland, S. Bhagat, Z. Trajanovic, M. Rajeswari, T. Venkatesan, A. Kratz, R. D. Gomez, and R. Ramesh, *J. Magn. Magn. Mater.* **172**, 229 (1997).
- [31] G. Luo, J. Lin, W.-C. Chiang, and C.-R. Chang, *Sci. Rep.* **7**, 6612 (2017).
- [32] Q. Qin, S. He, W. Song, P. Yang, Q. Wu, Y. P. Feng, and J. Chen, *Appl. Phys. Lett.* **110**, 112401 (2017).
- [33] P. Gupta, B. B. Singh, K. Roy, A. Sarkar, M. Waschke, T. Brueckel, and S. Bedanta, *Nanoscale* **13**, 2714 (2021).
- [34] G. Luo, C. Chang, and J. Lin, *J. Appl. Phys.* **115**, 17C508 (2014).
- [35] H. K. Lee, I. Barsukov, A. Swartz, B. Kim, L. Yang, H. Hwang, and I. Krivorotov, *AIP Adv.* **6**, 055212 (2016).
- [36] P. Gupta, B. B. Singh, A. Mishra, A. Kumar, A. Sarkar, M. Waschke, and S. Bedanta, in *SPIN* (World Scientific, Singapore, 2023), p. 2340019.
- [37] B. B. Singh, S. K. Jena, M. Samanta, K. Biswas, B. Satpati, and S. Bedanta, *Phys. Status Solidi (RRL)* **13**, 1800492 (2019).
- [38] G. Luo, C. Chang, and J. Lin, *IEEE Trans. Magn.* **49**, 4371 (2013).
- [39] R. Iguchi and E. Saitoh, *J. Phys. Soc. Jpn.* **86**, 011003 (2017).
- [40] A. Conca, B. Heinz, M. R. Schweizer, S. Keller, E. T. Papaioannou, and B. Hillebrands, *Phys. Rev. B* **95**, 174426 (2017).
- [41] Y.-H. Huang, Y.-C. Weng, C.-T. Liang, and J. Lin, *AIP Adv.* **10**, 015041 (2020).
- [42] A. Azevedo, R. O. Cunha, F. Estrada, O. Alves Santos, J. B. S. Mendes, L. H. Vilela-Leão, R. L. Rodríguez-Suárez, and S. M. Rezende, *Phys. Rev. B* **92**, 024402 (2015).
- [43] Y. Tserkovnyak, A. Brataas, G. E. W. Bauer, and B. I. Halperin, *Rev. Mod. Phys.* **77**, 1375 (2005).

- [44] P. Saadatkia, P. Stepanov, and F. Selim, *Mater. Res. Express* **5**, 016202 (2018).
- [45] P. Giannozzi, O. Andreussi, T. Brumme, O. Bunau, M. B. Nardelli, M. Calandra, R. Car, C. Cavazzoni, D. Ceresoli, M. Cococcioni, N. Colonna, I. Carnimeo, A. Dal Corso, S. de Gironcoli, P. Delugas, R. A. DiStasio Jr., A. Ferretti, A. Floris, G. Fratesi, G. Fugallo *et al.*, *J. Phys.: Condens. Matter* **29**, 465901 (2017).
- [46] P. Giannozzi, S. Baroni, N. Bonini, M. Calandra, R. Car, C. Cavazzoni, D. Ceresoli, G. L. Chiarotti, M. Cococcioni, I. Dabo, A. Dal Corso, S. de Gironcoli, S. Fabris, G. Fratesi, R. Gebauer, U. Gerstmann, C. Gougoussis, A. Kokalj, M. Lazzeri, L. Martin-Samos *et al.*, *J. Phys.: Condens. Matter* **21**, 395502 (2009).
- [47] P. Giannozzi, O. Baseggio, P. Bonfà, D. Brunato, R. Car, I. Carnimeo, C. Cavazzoni, S. De Gironcoli, P. Delugas, F. Ferrari Ruffino, A. Ferretti, N. Marzari, I. Timrov, A. Urru, and S. Baroni, *J. Chem. Phys.* **152**, 154105 (2020).
- [48] G. Pizzi, V. Vitale, R. Arita, S. Blügel, F. Freimuth, G. Géranton, M. Gibertini, D. Gresch, C. Johnson, T. Koretsune, J. Ibañez-Azpiroz, H. Lee, J.-M. Lihm, D. Marchand, A. Marrazzo, Y. Mokrousov, J. I. Mustafa, Y. Nohara, Y. Nomura, L. Paulatto *et al.*, *J. Phys.: Condens. Matter* **32**, 165902 (2020).
- [49] J. Qiao, J. Zhou, Z. Yuan, and W. Zhao, *Phys. Rev. B* **98**, 214402 (2018).
- [50] S. S. Tsirkin, *npj Comput. Mater.* **7**, 33 (2021).
- [51] T. Nan, T. Anderson, J. Gibbons, K. Hwang, N. Campbell, H. Zhou, Y. Dong, G. Kim, D. Shao, T. Paudel, N. Reynolds, X. J. Wang, N. X. Sun, E. Y. Tsymbal, S. Y. Choi, M. S. Rzchowski, Y. B. Kim, D. C. Ralph, and C. B. Eom, *Proc. Natl. Acad. Sci. USA* **116**, 16186 (2019).
- [52] Y. Ou, Z. Wang, C. S. Chang, H. P. Nair, H. Paik, N. Reynolds, D. C. Ralph, D. A. Muller, D. G. Schlom, and R. A. Buhrman, *Nano Lett.* **19**, 3663 (2019).
- [53] P. Jadaun, L. F. Register, and S. K. Banerjee, *Proc. Natl. Acad. Sci. USA* **117**, 11878 (2020).